



# Near-GHz scanned-wavelength-modulation spectroscopy for MHz thermometry and H<sub>2</sub>O measurements in aluminized fireballs of energetic materials

Garrett Mathews<sup>1</sup> · Christopher Goldenstein<sup>1</sup>

Received: 27 June 2020 / Accepted: 27 September 2020 / Published online: 29 October 2020  
© Springer-Verlag GmbH Germany, part of Springer Nature 2020

## Abstract

This manuscript presents the development of a two-color laser-absorption-spectroscopy (LAS) sensor capable of providing calibration-free measurements of temperature and H<sub>2</sub>O at 1 MHz in particle-laden combustion environments. This sensor employs scanned-wavelength-modulation spectroscopy with first-harmonic-normalized second-harmonic detection (scanned-WMS-2f/1f) with two distributed-feedback (DFB) tunable diode lasers (TDLs) emitting near 1392 nm and 1469 nm. The wavelength of each laser was modulated at 35 or 45.5 MHz to frequency multiplex the lasers and, more importantly, enable simultaneous wavelength scanning across the peak of each H<sub>2</sub>O absorption transition at 1 MHz. This method provides an absolute, in situ wavelength reference which improves measurement accuracy and robustness. Methods to characterize the lasers' wavelength and intensity modulation at frequencies above 10 MHz are presented. Measurements of temperature and H<sub>2</sub>O mole fraction within 0.3–2.5% and 2–10%, respectively, of known values were acquired in a static-gas cell at temperatures of 700–1200 K. The sensor was applied to measure the path-integrated temperature and H<sub>2</sub>O column density in fireballs produced by igniting 0.75 g of grade 3, class B HMX with and without H-5 micro-aluminum powder (20% by mass). Temperature measurements were acquired in the fireballs with a 1- $\sigma$  precision of 50 K, 30 K, and 15 K for measurement rates of 1 MHz, 250 kHz, and 25 kHz, respectively. The results are the first to demonstrate that calibration-free measurements of gas properties can be acquired at 1 MHz using WMS-2f/1f.

## 1 Introduction

Fireballs of detonated and/or suspended energetic materials are utilized in a variety of important defense applications (e.g., to destroy chemical and biological weapons of mass destruction). Such fireballs represent an extremely complex and hostile combustion environment, often consisting of strong shock waves and turbulent, multi-phase combustion. A variety of high-speed optical diagnostics are needed to understand the combustion chemistry and physics governing these environments, as well as provide validation data for models used to predict the performance and behavior of such applications. Unfortunately, fireballs present several challenges which complicate the use of optical diagnostics, namely large optical transmission losses (e.g., from

particulate scattering), high luminosity and opacity, beam-steering and, in field-scale tests, the need to utilize fiber-coupled optical equipment or large standoff distances [1, 2]. These challenges are exacerbated when aluminum is added to energetic material charges [1, 2], which is often done to increase combustion performance and increase the gas temperature [3, 4].

Optical diagnostics have been widely utilized to measure various parameters in fireballs of energetic materials. Emission spectroscopy of AIO has been used to determine the temperature of aluminum combustion products [5–8], and broadband, single-shot, dye-laser-absorption measurements of Al, Ti, and AIO [9] and temperature via AlF and MgF [10] have been acquired in fireball environments. Several laser-absorption diagnostics operating in the near- and mid-infrared have also been utilized to characterize post-detonation gases and explosive blasts [11–13]. Carney et al. [11] used a broadband near-infrared light source and a spectrometer to measure H<sub>2</sub>O absorbance spectra between 1335 and 1380 nm and determine temperature and H<sub>2</sub>O concentration at 20 kHz in the expansion of a high-explosive

✉ Garrett Mathews  
gmathew@purdue.edu

<sup>1</sup> School of Mechanical Engineering, Purdue University, 585 Purdue Mall, West Lafayette, IN 47906, USA

detonation. Murzyn et al. [12] utilized a rugged fiber-optic probe and scanned-wavelength direct absorption with near-infrared tunable diode lasers (TDLs) to measure temperature and  $\text{H}_2\text{O}$  at up to 30 kHz in air that was shock heated via an explosive blast wave in a constant volume chamber. Most recently, Phillips et al. [13] utilized an external-cavity quantum-cascade laser (EC-QCL) to measure path-integrated concentrations of CO,  $\text{CO}_2$ ,  $\text{H}_2\text{O}$ , and  $\text{N}_2\text{O}$  (via absorbance spectra from 2050 to 2300  $\text{cm}^{-1}$ ) at a repetition rate of 100 Hz in post-detonation gases of explosives. In addition, the authors acquired measurements of fireball emission and transmission at 500 kHz. Despite this prior work, diagnostics that can provide temperature and species measurements at rates approaching 1 MHz in harsh, optically dense fireball environments remain needed to quantify rapid transients in gas conditions and, perhaps, to improve measurement quality by enabling time averaging on short timescales.

Laser-absorption spectroscopy (LAS) has been widely used to achieve measurement rates of 10 s of kHz (see [14] and references therein); however, far fewer LAS diagnostics have been able to achieve a measurement rate of 100 kHz or greater (excluding fixed-wavelength LAS diagnostics which are significantly less robust and generally not preferred in harsh combustion environments [14]). To mention a few examples, a broadly and rapidly tunable MEMS VCSEL emitting near 1350 nm has been used to provide temperature and  $\text{H}_2\text{O}$  measurements at 100 kHz in a rotating-detonation combustor [15]. In addition, recently several researchers have utilized quantum-cascade lasers to achieve measurement rates of 100 kHz and beyond via direct absorption spectroscopy. For example, Rein et al. utilized three time-division-multiplexed QCLs to measure temperature, CO,  $\text{CO}_2$ , and  $\text{N}_2\text{O}$  at 100 kHz in detonation gases [16]. More recently, Naasir and Farooq used an intrapulse approach to measure gas temperature at 100 kHz in high-pressure (15–20 atm) gases within a rapid-compression machine by using two pulsed QCLs emitting near 5.46 and 5.60  $\mu\text{m}$  [17]. In comparison, Pineda et al. [18] scanned the wavelength of a continuous-wave QCL across five rovibrational absorption transitions near 2008  $\text{cm}^{-1}$  to measure temperature,  $^{12}\text{CO}$  and  $^{13}\text{CO}$  concentrations simultaneously at 100 kHz in shock tube experiments to study reaction kinetics of isotopically labeled hydrocarbon mixtures. Regarding LAS measurements conducted at rates greater than 100 kHz, Chrystie et al. used a pulsed-QCL emitting near 7.6  $\mu\text{m}$  to generate frequency-chirped pulses and provide intrapulse measurements of  $\text{H}_2\text{O}$  absorbance spectra and temperature in shock-tube gases at a repetition rate of 250 kHz [19]. Most recently, Nair et al. [20] developed a scanned-wavelength direct-absorption-spectroscopy (scanned-DAS) diagnostic for measuring temperature, CO column density, and pressure at 1 MHz in detonation gases. The wavelength of a QCL

was scanned across a cluster of CO transitions near 2008.5  $\text{cm}^{-1}$  spanning three vibrational levels for high-temperature sensitivity. Measurements were demonstrated in a methane–oxygen-fueled rotating detonation rocket engine.

While highly useful, all of the aforementioned LAS techniques utilized direct-absorption techniques which can suffer from higher noise levels (compared to wavelength/frequency modulation techniques) and they all rely on the ability to infer the baseline light intensity. The latter of which can be extremely difficult, particularly in cases with large optical transmission losses and at elevated pressures where collisional broadening can prevent in situ determination of a non-resonant baseline intensity. As a result, ultra-high-bandwidth (> 100 kHz) LAS diagnostics employing wavelength/frequency modulation spectroscopy (WMS or FMS) remain needed.

Wavelength-modulation spectroscopy (WMS) is a LAS technique often utilized to improve measurement precision by rejecting noise and canceling out intensity fluctuations due to non-absorbing losses in harsh, optically dense environments [21, 22]. While numerous high-bandwidth ( $\geq 10$  kHz) WMS sensors have been deployed in combustion environments [23–28], to our knowledge WMS diagnostics providing a measurement bandwidth greater than 100 kHz have not been previously developed. In addition, most of the high-bandwidth WMS diagnostics have employed fixed-WMS techniques [23–25] which are susceptible to laser drift (particularly at low to moderate pressures where absorption lines are narrow) and, potentially, unknown pressure shifting of the transition linecenter. For these reasons, work has been done to develop high-bandwidth scanned-WMS diagnostics to provide an in situ wavelength reference via measurement of WMS spectra. For example, Goldenstein et al. [27] developed a two-color, peak-picking scanned-WMS- $2f/1f$  diagnostic to provide measurements of temperature and  $\text{H}_2\text{O}$  concentration at 50 kHz in the exhaust of a rotating detonation engine. In this method, small amplitude wavelength scanning was performed sinusoidally at 25 kHz to resolve the peak WMS- $2f/1f$  signal at the transition linecenter at 50 kHz which required using modulation frequencies of 225 and 285 kHz. Alternatively, the wavelength of the laser can be scanned across an entire absorption line to enable scanned-WMS- $2f/1f$  spectral fitting [22] to be performed and avoid the need for temperature- and species-dependent collisional broadening models. Unfortunately, the large amplitude wavelength scanning that is required in combination with high-frequency wavelength modulation has limited this technique to measurement rates of 25 kHz using modulation frequencies approaching 1 MHz [22, 26]. That being said, achieving larger measurement rates via scanned-WMS requires using even larger modulation frequencies (typically at least 10–100x larger than the scan frequency).

This paper presents the development of a scanned-WMS- $2f/1f$  sensor capable of providing measurements of temperature and  $\text{H}_2\text{O}$  at 1 MHz and its initial application to characterizing laboratory-scale fireballs of HMX (1,3,5,7-tetranitro-1,3,5,7-tetrazoctane) with and without micro-aluminum particles. Several complications associated with performing ultra-high-frequency (i.e.,  $>10$  MHz) injection-current modulation of telecommunication-grade TDLs are addressed, and new laser-characterization techniques which enable calibration-free WMS measurements in this regime are presented. To the best of our knowledge, this work presents the first calibration-free WMS- $2f/1f$  sensor which is able to achieve a measurement rate of 1 MHz. This represents a  $10\times$  or  $20\times$  improvement in measurement rate compared to previously developed fixed-wavelength WMS (i.e., fixed-WMS) and scanned-WMS sensors, respectively.

## 2 Fundamentals of LAS and WMS

### 2.1 Laser-absorption spectroscopy

In LAS, laser light is directed through a test gas, and the transmitted light intensity at a given wavelength is measured and related to gas properties of the absorbing species via Beer's law, given by Eq. 1.

$$\frac{I_t(\nu)}{I_0(\nu)} = \exp[-\alpha(\nu)]. \quad (1)$$

Here  $I_t$  is the transmitted light intensity,  $I_0$  is the incident light intensity,  $\nu$  is the optical frequency, and  $\alpha$  is the spectral absorbance. If the gas conditions vary along the line-of-sight, the spectral absorbance is given by Eq. 2:

$$\alpha(\nu) = \int_0^L S(T)n_i\phi(\nu)dl \quad (2)$$

where  $S$  ( $\text{cm}^{-1}$ -molecules/ $\text{cm}^2$ ) is the transition linestrength,  $T$  (K) is the gas temperature,  $n_i$  (molecules/ $\text{cm}^3$ ) is the absorbing species number density,  $\phi$  (cm) is the transition lineshape,  $dl$  is a differential length element, and  $L$  (cm) is the total path length through the absorbing gas. A Voigt profile is typically used to model the lineshape and accounts for both Doppler and collisional broadening [29]. The integrated absorbance of a given transition  $j$ ,  $A_j$ , is given by Eq. 3:

$$A_j = \int_\nu \int_0^L S_j(T)n_i\phi(\nu)dld\nu = \int_0^L S_j(T)n_i dl, \quad (3)$$

which removes dependence on the transition lineshape since it has an area of unity.

For a nonuniform line-of-sight, the two-color ratio of  $A_j$  or  $\alpha(\nu)$  can be used to calculate a path-integrated temperature

of the absorbing species and a measurement of  $A_j$  or  $\alpha(\nu)$  from a single transition can then be used to determine a path-integrated species number density or concentration, both of which depend on the spectroscopic parameters and distribution of gas properties along the line-of-sight, the latter of which is typically unknown. That being said, if the linestrength of each transition exhibits a linear dependence on temperature (across the range of the temperature nonuniformity), the temperature inferred from comparing the measured two-color ratio of  $A_j$  with that simulated assuming a uniform line-of-sight is precisely equal to the absorbing-species number-density-weighted path-averaged temperature given by Eq. 4 [30].

$$\bar{T}_{n_i} \equiv \frac{\int_0^L Tn_i dl}{\int_0^L n_i dl}. \quad (4)$$

Once  $\bar{T}_{n_i}$  is known, the absorbing-species column density,  $N_i$  (molecules/ $\text{cm}^2$ ), can be calculated from the measured  $A_j$  using Eq. 5.

$$N_i \equiv \int_0^L n_i dl = \frac{A_j}{S_j(\bar{T}_{n_i})}. \quad (5)$$

These relations are significant since they connect the path-integrated two-color measurements to physical quantities which can be more easily compared with those predicted by combustion models. Further, Eq. 4 clearly illustrates that the temperature inferred is inherently species specific when gradients in temperature and species concentration are present along the line-of-sight.

### 2.2 Scanned-WMS- $2f/1f$

In scanned-WMS- $2f/1f$ , the nominal wavelength of the laser is scanned across an absorption line or portion thereof while the laser's wavelength is simultaneously modulated at a much higher frequency. The wavelength modulation encodes absorption information at harmonics of the modulation frequency which are typically more isolated from noise [31], and the wavelength scanning provides spectrally resolved measurements of the WMS harmonic signals (e.g.,  $1f$ ,  $2f$ ) [22, 32] which are extracted from the raw detector signal using lock-in amplifiers or filters. The  $2f$  signal is normalized by the  $1f$  signal to actively account for non-absorbing transmission losses produced by, for example, beamsteering, particulate scattering, and window fouling [33].

Here, the peak scanned-WMS- $2f/1f$  signal at linecenter,  $S_{2f/1f}(\nu_o)$ , was used to determine the path-integrated temperature and concentration or column density of  $\text{H}_2\text{O}$ . This was achieved by comparing measured signals with those predicted as a function of gas properties using the calibration-free WMS- $2f/1f$  model developed by Rieker et al. [21]. That

said, in the interest of clarity and brevity the most pertinent fundamental relationships governing  $S_{2f/1f}(v_o)$  will be discussed under simplified conditions that are appropriate for the measurements reported here. For an optically thin gas ( $\alpha < 0.05$ ) using a laser with first-order intensity modulation and a phase-shift between intensity and wavelength modulation of  $\pi$ ,  $S_{2f/1f}(v_o)$  is given by Eq. 6 for a nonuniform line-of-sight.

$$S_{2f/1f}(v_o) \approx \frac{1}{i_0\pi} \int_{-\pi}^{\pi} \int_0^L S(T)n_i \times \phi(v_o + a\cos(\theta))d\ell\cos(2\theta)d\theta. \quad (6)$$

Here,  $i_0$  is the DC-intensity-normalized intensity-modulation amplitude and  $a$  is the frequency modulation amplitude (i.e., the modulation depth) of the laser. In this limit,  $S_{2f/1f}(v_o)$  scales linearly with absorbance for a given lineshape and modulation depth and, as a result, traditional absorption-spectroscopy relationships can be exploited to determine gas properties. For example, for a uniform line-of-sight the two-color ratio of  $S_{2f/1f}(v_o)$  can be used to determine the gas temperature since it is nearly a function of temperature only, exhibiting only a weak dependence on pressure and composition through the lineshape which can be accounted for via iteration. Similarly, with temperature, pressure, and path length known,  $S_{2f/1f}(v_o)$  can be used to determine the absorbing species mole fraction [21].

For a nonuniform line-of-sight, the two color ratio of  $S_{2f/1f}(v_o)$  can be used to determine  $\bar{T}_{n_i}$ , and  $N_i$  can then be determined from  $S_{2f/1f}(v_o)$  from either laser if: (1) two transitions with linestrengths that exhibit a linear temperature dependence are used and (2) the path-integrated lineshape can be determined in situ (e.g., via spectral fitting) and then constrained in the WMS model used to simulate  $S_{2f/1f}(v_o)$  as a function of temperature [30]. In these limits,  $S_{2f/1f}(v_o)$  scales linearly with  $A_j$  and known or empirically derived constants. As such,  $\bar{T}_{n_i}$  and  $N_i$  can be obtained analogous to as described for direct absorption in Sect. 2.1 [30]. While the aforementioned requirements could not be precisely met here, synthetic (i.e., simulated) measurements suggest that the temperature inferred from the two-color ratio of  $S_{2f/1f}(v_o)$  measured in HMX fireballs will agree within 1–4% of  $\bar{T}_{n_i}$ . Similarly, the column density inferred from  $S_{2f/1f}(v_o)$  of either laser is expected to agree within 2–4.5% of  $N_{H_2O}$  depending on  $\bar{T}_{n_i}$  and the line-of-sight nonuniformities encountered. The synthetic path-integrated measurements of  $S_{2f/1f}(v_o)$  were generated following the approach described by Goldenstein et al. [30, 34] using the calibration-free WMS model developed by Rieker et al. [21] and estimated line-of-sight distributions for temperature and  $H_2O$  that are representative of those expected in HMX fireballs.

It is also important to note that the magnitude of the WMS harmonic signals is influenced by the modulation

depth. In scanned-WMS- $2f/1f$  performed with injection-current-tuned lasers and small absorbance ( $\alpha < 1$ ), the  $1f$  signal is dominated by intensity modulation of the laser and is primarily used for simply normalizing out variations in light intensity. In contrast, the  $2f$  signal is dominated by the spectral absorbance and a sufficient modulation depth is required to maximize the  $2f$  signal. Specifically, a modulation index,  $m$  (i.e., the modulation depth divided by the transition half-width at half-maximum), of 2.2 is required to maximize the  $2f$  signal and larger values of  $m$  can be used to desensitize the  $2f$  signal to the transition lineshape [21]. This is particularly relevant as it may not be possible to achieve a modulation depth that is large enough to generate maximum  $2f$  signals, for example, when collisional broadening is large or when a sufficient wavelength-modulation amplitude cannot be achieved. Achieving a modulation depth large enough for maximizing the  $2f$  signal motivated the use of near-GHz modulation frequencies as discussed further in Sect. 3.

### 3 Advantages of near-GHz WMS

There are three primary advantages associated with performing WMS with near-GHz modulation frequencies. First, using higher modulation frequencies typically increases the signal-to-noise ratio (SNR). This can be understood by recognizing that using higher modulation frequencies encodes absorption information at higher frequencies where, for example, laser and detector noise are reduced [35]. This effect was demonstrated here by acquiring fixed-WMS- $2f/1f$  measurements of  $H_2O$  in ambient air using different modulation frequencies and lock-in filter bandwidths. Figure 1 shows the SNR of the WMS- $2f/1f$  signal at the linecenter of the  $H_2O$  absorption transition near  $7185.59 \text{ cm}^{-1}$ . The modulation index was held constant for each experiment. For a given lock-in filter bandwidth, the SNR increases as the modulation frequency increases. For example, using a modulation frequency of 50 MHz instead of 500 kHz improves the SNR by approximately a factor of 2 for a lock-in filter bandwidth of 100 kHz.

Second, using higher modulation frequencies enables higher measurement rates. This is most obvious in the case of fixed-WMS where the lock-in filter bandwidth dictates the measurement bandwidth of the sensor [27]. In this case, using higher modulation frequencies increases the separation between harmonics which in turn enables larger bandwidth lock-in filters to be used to extract the WMS harmonic signals. In scanned-WMS, the scan frequency dictates the measurement rate, and it must be  $\approx 10\text{--}100\times$  smaller than the modulation frequency depending on the scan amplitude [27]. It therefore follows that higher modulation frequencies enable higher scan frequencies to be used in order to achieve larger measurement rates.

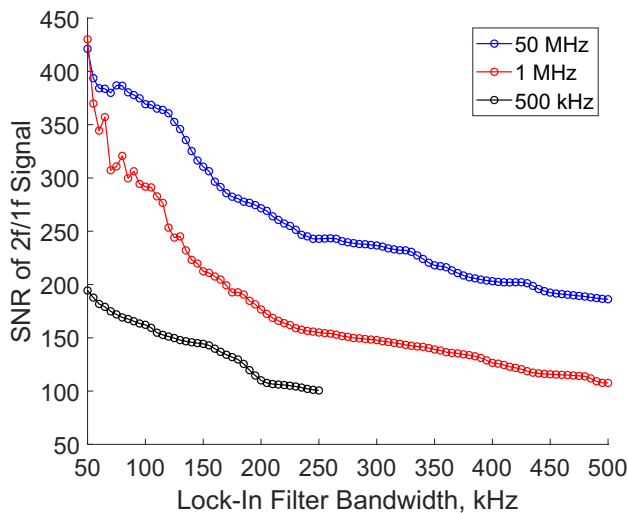


**Fig. 1** SNR as a function of lock-in filter bandwidth for the WMS- $2f/1f$  signal measured at the linecenter of the  $\text{H}_2\text{O}$  transition near  $7185.59 \text{ cm}^{-1}$  at atmospheric conditions. Increasing the modulation frequency increases the SNR of the signal for a given lock-in filter bandwidth

Third, performing WMS with near-GHz modulation frequencies (i.e.,  $f > 10 \text{ MHz}$ ) enables larger modulation depths to be achieved (in comparison to modulation frequencies near 1–10 MHz) with injection-current-tuned TDLs. This may be required to maximize the  $2f$  signal at the conditions of interest, particularly those with large collisional broadening [e.g., at number densities near or above those encountered at standard-temperature and pressure (STP)]. This somewhat surprising result originates from a transition from one laser-wavelength-tuning mechanism to another. For example, when injection-current tuning TDLs at frequencies less than 1 MHz the dominant wavelength-tuning mechanism is thermal expansion of the wavelength-selection grating which results from ohmic heating induced by the injection current. The efficiency of this mechanism degrades as the modulation frequency is increased which results in a decrease in wavelength tuning amplitude. However, at higher frequencies (i.e.,  $> 10 \text{ MHz}$ ), the wavelength tuning is dominated by carrier density modulation within the semiconductor which provides an increase in the wavelength-tuning amplitude. Carrier density modulation arises from coupling between the injection current and the electron and photon densities within the active region of the semiconductor laser. Modulation of the electron density changes the refractive index of the semiconductor resulting in frequency modulation (FM) of the laser's output. The FM frequency response of semiconductor lasers operating on interband transitions exhibits a resonance peak due to relaxation oscillation in the semiconductor resulting in enhanced FM at high modulation frequencies [36–39].

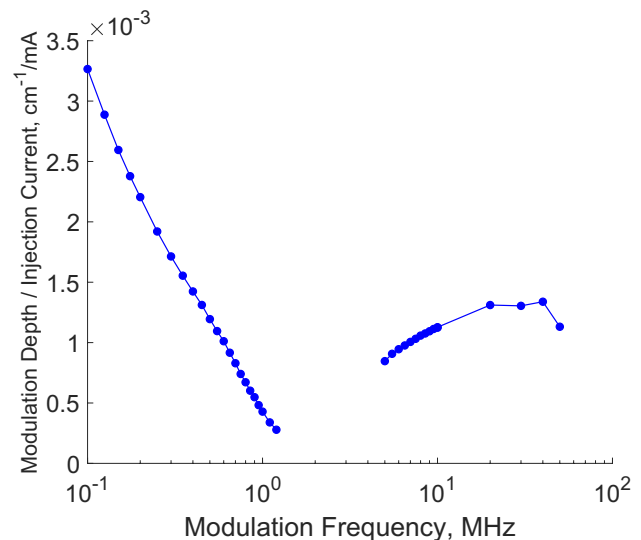


**Fig. 2** Modulation depth per unit injection-current amplitude that was applied to the TDL (results shown are for the TDL emitting near 1392 nm). The modulation depth decreases rapidly with increasing modulation frequency at frequencies less than 1 MHz. The modulation depth partially recovers and becomes nearly independent of modulation frequency at modulation frequencies between 10 and 50 MHz

Figure 2 illustrates the wavelength tuning response of our TDL emitting near 1392 nm while being injection-current modulated in these two regimes. The results show that the modulation depth decreases rapidly as the modulation frequency is increased to 1 MHz (the 3 dB bandwidth of the laser current controller). At modulation frequencies between 10 and 50 MHz (tested via injection-current modulation through a bias-T), the laser's modulation depth recovers to that which is achievable at 450 kHz via modulation applied directly to the laser-current controller. The modulation depth at frequencies from 3 to 10 MHz is limited by the frequency response of the bias-T circuit used to apply the injection-current modulation which has a cut-on frequency of 10 MHz. Carrier density modulation within the TDLs enables the near-GHz WMS diagnostic reported here to achieve maximum  $2f$  signals in combustion gases at 1 atm while using modulation frequencies that are large enough to provide scanned-WMS- $2f/1f$  measurements of temperature and  $\text{H}_2\text{O}$  at 1 MHz.

It should be noted that as  $f$  is increased to frequencies that are comparable to the transition HWHM (i.e., near-GHz levels at STP), dispersion can significantly alter the WMS harmonic signals [35, 40] and traditional laser-characterization techniques are no longer practical; the latter is discussed in Sect. 6. Regarding the former, we recently developed a new calibration-free model to account for the influence of optical dispersion upon WMS or FMS signals [40]. This model is analogous to the scanned-WMS model developed by Goldenstein et al. [22]; however, the new model retains

optical phase information by simulating how a wavelength/frequency-modulated electric field is absorbed and dispersed in the presence of an absorption line. As a result, this approach is valid across a wide range of modulation frequencies (e.g., kHz–GHz). Simulations performed with this model showed that dispersion has a negligible impact on the WMS- $2f/1f$  signals measured here using modulation frequencies of 35 and 45.5 MHz. As a result, traditional calibration-free WMS- $2f/1f$  models were used here due to their reduced complexity.

## 4 Sensor design

### 4.1 Line selection

Two TDLs emitting near  $1.4\ \mu\text{m}$  were used to access the  $\text{H}_2\text{O}$  absorption transitions near  $7185.59\ \text{cm}^{-1}$  and  $6806.03\ \text{cm}^{-1}$ . The most pertinent spectroscopic parameters for these transitions are provided in Table 1. These transitions were used due to: (1) the high temperature sensitivity provided by this pair of lines, (2) availability of spectroscopic parameters that were experimentally validated at high temperatures [27], (3) isolation from interfering absorption transitions, and (4) sufficiently strong absorption levels expected at the gas conditions and scales of interest.

Figure 3 shows simulated absorbance spectra of  $\text{H}_2\text{O}$  for the transitions of interest at conditions representative of those encountered in HMX fireballs ( $T = 2800\ \text{K}$ ,  $X_{\text{H}_2\text{O}} = 0.2$ ,  $P = 1\ \text{atm}$ ,  $L = 10\ \text{cm}$ ). At these conditions, the spectral absorbance at linecenter is 0.042 and 0.029 for the transition near  $7185.59$  and  $6806.03\ \text{cm}^{-1}$ , respectively. Absorbance spectra and WMS- $2f/1f$  signals were simulated using the spectroscopic model described by Goldenstein et al. [42] in combination with the HITRAN2012 database [41] and experimentally refined linestrengths,  $\text{N}_2$ - and  $\text{H}_2\text{O}$ -broadening parameters for the transitions near  $7185.59\ \text{cm}^{-1}$  and  $6806.03\ \text{cm}^{-1}$  (see Table 1) which were taken from [27].

**Table 1** Spectroscopic parameters for dominant  $\text{H}_2\text{O}$  transitions

Parameter	Transition	
$\nu_o, \text{cm}^{-1}$	7185.59 <sup>a</sup>	6806.03 <sup>a</sup>
$S(296\ \text{K}), \text{cm}^{-2}/\text{atm}$	$1.96 \times 10^{-2}$	$6.40 \times 10^{-7}$
$E'', \text{cm}^{-1}$	1045.1	3291.2
$\gamma_{\text{N}_2}(296\ \text{K}), \text{cm}^{-1}/\text{atm}$	0.045	0.0105
$n_{\text{N}_2}$	0.51	-0.108
$\gamma_{\text{H}_2\text{O}}(296\ \text{K}), \text{cm}^{-1}/\text{atm}$	0.198	0.205
$n_{\text{H}_2\text{O}}$	0.53	0.86

$\nu_o$  and  $E''$  taken from HITRAN2012 [41]

All other parameters taken from [27]

<sup>a</sup>Denotes a doublet transition

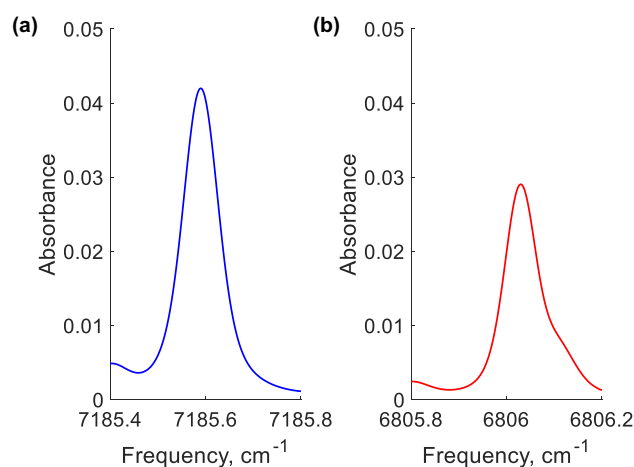


**Fig. 3** Simulated absorbance spectra for the  $\text{H}_2\text{O}$  absorption transitions near  $7185.6\ \text{cm}^{-1}$  (a) and  $6806.0\ \text{cm}^{-1}$  (b) at gas conditions representative of the HMX fireballs studied here ( $T = 2800\ \text{K}$ ,  $P = 1\ \text{atm}$ ,  $X_{\text{H}_2\text{O}} = 0.2$ ,  $L = 10\ \text{cm}$ )

Neighboring absorption transitions located from  $7184.10$  to  $7187.00\ \text{cm}^{-1}$  and from  $6805.16$  to  $6807.10\ \text{cm}^{-1}$  were also included in the simulation to account for their far-wing absorption near the dominant transitions; however, this has a minor ( $<1\%$ ) impact on the absorbance at linecenter for the dominant transitions. The transition collisional widths were modeled assuming a binary mixture of  $\text{H}_2\text{O}$  in  $\text{N}_2$  (for dominant transitions) or air (for all other transitions) due to the limited availability of collisional-broadening coefficients.

### 4.2 Selection of WMS technique

A scanned-WMS- $2f/1f$  technique employing small amplitude wavelength scanning and near-GHz modulation frequencies was used for three primary reasons. First, WMS- $2f/1f$  was used to (i) account for optical transmission losses induced by particulate scattering and beamsteering in HMX fireballs and (ii) to provide high-SNR measurements despite relatively small absorbance ( $< 0.05$ ) and large environmental noise. Second, near-GHz modulation frequencies were used to leverage the advantages discussed in Section 3, primarily, to enable two-color scanned-WMS- $2f/1f$  measurements of temperature and  $\text{H}_2\text{O}$  be acquired at 1 MHz while also avoiding the need to use GHz electronics. Third, small amplitude wavelength scanning was performed to (i) improve measurement accuracy and robustness by providing an in situ wavelength reference (the peak WMS- $2f/1f$  signal at linecenter) and (ii) to enable lock-in filters to be used with a minimum bandwidth [i.e., a bandwidth near equal to the measurement rate (1 MHz here)]. This is not possible when trying to resolve the entire WMS- $2f/1f$  spectrum which requires use of much larger bandwidth lock-in filters [27] which inherently pass more noise.

## 5 Experimental setup and procedures

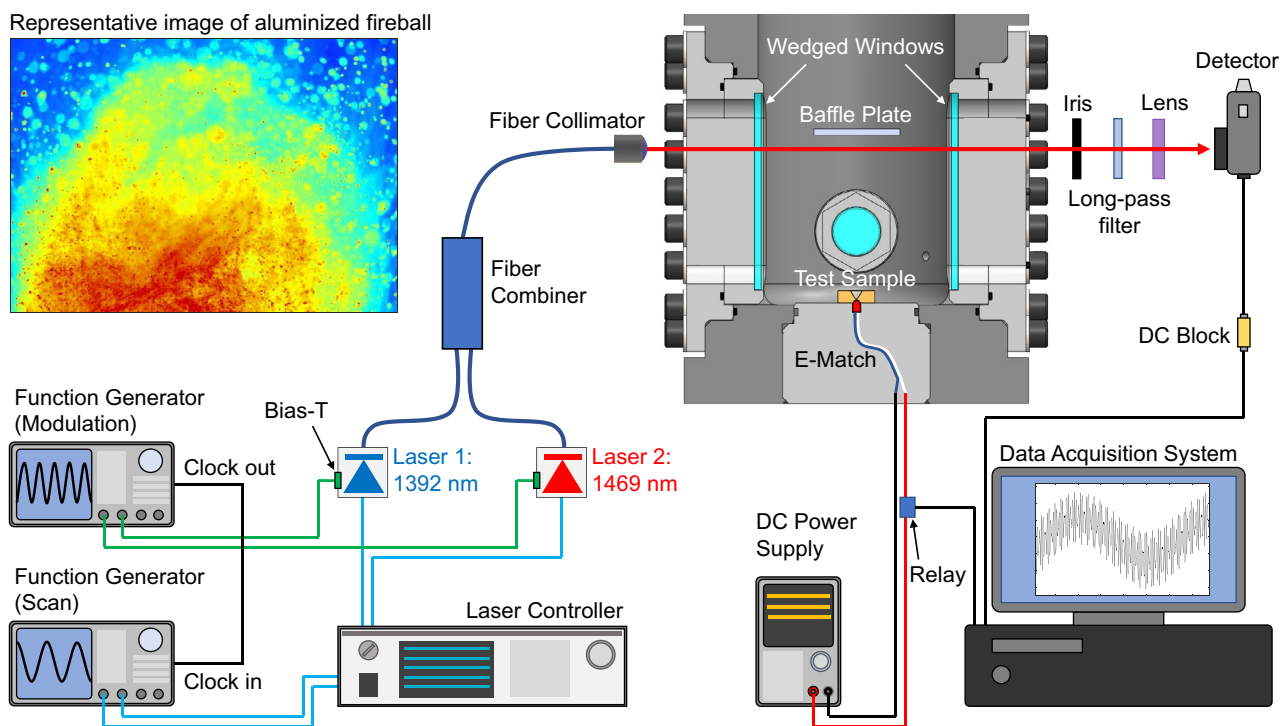
### 5.1 Optical equipment

Figure 4 illustrates a schematic of the experimental setup used to characterize fireballs of HMX. Two fiber-coupled, distributed-feedback TDLs (NTT Electronics) were used to access the  $\text{H}_2\text{O}$  transitions near  $7185.59\text{ cm}^{-1}$  and  $6806.03\text{ cm}^{-1}$ . The lasers were mounted in butterfly-type laser mounts (ILX Lightwave LDM-4984-BTB) with bias-T inputs to accommodate high-frequency modulation, and the lasers' temperature and current were controlled with a commercial laser controller (ILX Lightwave LDC-3908). The wavelength and intensity of the lasers emitting near 1392 and 1469 nm were injection-current modulated at 35 MHz and 45.5 MHz (via the bias-T) with modulation depths of  $0.107\text{ cm}^{-1}$  and  $0.082\text{ cm}^{-1}$ , respectively. In addition, simultaneous injection-current scanning was performed through the laser controller using a 500 kHz sinewave. Frequency-scanning amplitudes of  $0.045\text{ cm}^{-1}$  and  $0.040\text{ cm}^{-1}$  were utilized. Two 240 MHz bandwidth, two-channel, arbitrary function generators (Tektronix AFG-3252) were used to produce the waveforms that were used to scan and modulate the wavelength of each laser. The first AFG generated both modulation waveforms and output a 10 MHz reference clock signal which was used to

synchronize both AFGs. The second AFG generated both scan waveforms.

The light emitted by the two TDLs was combined into a single fiber using a fiber combiner/splitter, and the output was collimated (Thorlabs F240APC-C) to a beam diameter of 1.7 mm and pitched through the test gas within a gas cell (see Sect. 5.2) or combustion chamber (see Sect. 5.3). The transmitted laser light was directed through a 6.5-mm-diameter iris and a long-pass spectral filter (Thorlabs FELH1350) with a cut-on wavelength of 1350 nm was used to prevent detector saturation in tests involving aluminized HMX fireballs. The laser light was then collected using a 25.4-mm-diameter, 40-mm focal length, anti-reflection coated lens (Thorlabs LA1422-C) and directed onto a photodetector with a 3dB bandwidth of 150 MHz (Thorlabs PDA10CF). The detector signal was AC coupled using a DC block (Crystek CBLK-300-3) with a passband from 300 kHz to 3 GHz and recorded at 3 GS/s using a 12-bit data acquisition card (GaGe CSE123G2) with a  $\pm 1\text{ V}$  dynamic range. The WMS-1f and -2f signals were extracted from the raw detector signal during post-processing using lock-in filters with a 1.1 MHz bandwidth.

In addition, scanned-WMS-2f/1f measurements were also acquired in a static-gas cell while using more conventional scan and modulation frequencies (100× smaller than the near-GHz scanned-WMS-2f/1f diagnostic reported here) to further evaluate the SNR enhancement provided by



**Fig. 4** Schematic of experimental setup used to characterize fireballs of HMX and micro-aluminum with the scanned-WMS-2f/1f diagnostic

modulating at near-GHz frequencies. Specifically, the two TDLs emitting near 1392 nm and 1469 nm were injection current modulated at 350 kHz and 455 kHz with modulation amplitudes of  $0.107 \text{ cm}^{-1}$  and  $0.085 \text{ cm}^{-1}$ , respectively, while being simultaneously sinusoidally scanned at 5 kHz with scan amplitudes of  $0.044 \text{ cm}^{-1}$  and  $0.043 \text{ cm}^{-1}$ , respectively. In this operation mode the WMS- $2f/1f$  signals were extracted from the detector signal using lock-in filters with a bandwidth of 11 kHz (i.e., 100x smaller than that used to acquire 1 MHz measurements with near-GHz modulation frequencies).

## 5.2 High-temperature gas cell

The accuracy of the scanned-WMS- $2f/1f$  diagnostic was evaluated by acquiring measurements of gas temperature and  $\text{H}_2\text{O}$  concentration in a static-gas cell. The gas cell is thoroughly described by Schwarm et al. [43], most critically it is equipped with 0.5 inch diameter, 4-inch-long sapphire rods with a  $1^\circ$  wedged face to provide an optical path length of 9.7 cm. Sapphire rods were used instead of  $\text{CaF}_2$ , since  $\text{CaF}_2$  reacts with  $\text{H}_2\text{O}$  at the high-temperatures of interest here. The gas cell was heated to temperatures from 700 to 1200 K in a high-uniformity tube furnace, and the temperature was maintained within  $\pm 5$  K (measured by three equally spaced type-K thermocouples) across the measurement path. For each test condition, the gas cell was evacuated to a pressure  $< 1$  mBar and then filled with pure  $\text{H}_2\text{O}$  up to its vapor pressure at room temperature ( $\approx 30$  mBar). After which, the cell was filled with ambient air ( $\approx 1\%$   $\text{H}_2\text{O}$  by mole) up to 1 atm. This procedure was employed to increase the concentration of  $\text{H}_2\text{O}$  in the cell above that which is achievable via thermodynamic phase equilibrium at room temperature. Laser light was directed through the gas cell as described in Sect. 5.

## 5.3 Combustion chamber and fireballs

Fireballs were produced in Purdue's high-pressure combustion chamber (HPCC) which is described thoroughly by Tancin et al. [44] and shown in Fig. 4. A 3-D printed sample holder with a conical cavity was secured to the base of the HPCC and held samples consisting of (1) 0.75 g of grade 3, class B HMX powder or (2) 0.60 g of grade 3, class B HMX powder and 0.15 g of H-5 micro-aluminum powder (4.5–7.0  $\mu\text{m}$  diameter particles). An electric match (i.e., e-match) was inserted into the bottom of the sample holder and used to ignite the test samples. A 5 A current generated by a DC power supply (Rigol DP711) was passed through an electric relay (Songle SRD-05VDC-SL-C) and used to ignite the e-match with precise timing.

The line-of-sight for the scanned-WMS- $2f/1f$  measurements was directed across the HPCC approximately 12.5

cm above the sample holder. A 5- $\text{cm}^2$  aluminum baffle plate was placed 15 cm above the sample holder to promote fireball expansion and increase the optical path length through the fireball to a maximum diameter of  $\approx 15$  cm. Before each test, the HPCC was sealed and evacuated to near vacuum and then filled with dry air to 1 atm. This procedure was followed such that there was no water vapor in the chamber prior to initiating combustion. As a result, the path-integrated scanned-WMS- $2f/1f$  measurements are not influenced by the gas conditions outside of the fireball. Prior to igniting the sample, the top plug of the HPCC was removed and replaced with an exhaust duct to enable the fireball to escape the chamber and provide a near-constant-pressure test.

## 6 Laser and detector characterization

Calibration-free WMS models require accurate submodels describing the wavelength and intensity modulation of the laser in order to simulate WMS- $2f/1f$  signals as a function of gas conditions [21, 22]. In this work, the calibration-free WMS models developed by Rieker et al. [21] and Goldenstein et al. [22] were utilized and these models both assume sinusoidal frequency (first order only) and intensity (first and second order) modulation according to Eqs. 7 and 8, respectively.

$$v(t) = \bar{v} + a \cos(2\pi ft) \quad (7)$$

$$I_0(t) = \bar{I}_0 (1 + i_0 \cos(2\pi ft + \psi) + i_2 \cos(4\pi ft + \psi_2)). \quad (8)$$

Here,  $\bar{v}$  is the nominal frequency of the laser,  $a$  is the modulation depth,  $\bar{I}_0$  is the DC light intensity,  $i_0$  and  $i_2$  are the first- and second-order DC-normalized intensity-modulation amplitudes, and  $\psi$  and  $\psi_2$  are the phase shift between first- and second-order intensity modulation and frequency modulation. These parameters are required inputs into the calibration-free WMS models used here. It is important to note that Eqs. 7 and 8 only account for the modulation waveform and, thus, ignore the influence of injection-current scanning which can be accounted for using the model developed by Goldenstein et al. [22]. This was done to determine  $\psi$  as described in Sect. 6.2.

Methods for characterizing the frequency and intensity modulation of TDLs using modulation frequencies up to several MHz and in the absence of simultaneous injection-current scanning have been well-documented [45]. In this case, a Fabry-Perot etalon can be used to quantify the laser's frequency modulation amplitude by resolving the interference fringes (i.e., peaks) that occur each time the laser's frequency has tuned one free-spectral range (FSR) of the etalon. Increasing the modulation frequency beyond several MHz requires utilizing a GHz detector to accurately resolve



the many peaks produced within each period of modulation and even this becomes impractical at modulation frequencies beyond 10 MHz. Further, at such high modulation frequencies slight differences in the time-of-flight of the laser light across multiple paths or optical instruments severely complicates determination of the phase difference between intensity and frequency modulation using traditional WMS laser-characterization methods [45]. Last, the presence of simultaneous high-frequency injection-current scanning introduces a time-varying intensity-modulation amplitude which must be accounted for [22].

This section thoroughly describes experimental procedures and data processing methods (similar to those used in FMS) for inferring the necessary parameters describing the laser's frequency and intensity modulation, specifically,  $a$ ,  $\psi$ , and a time-varying  $i_0$ . In addition, methods for quantifying the frequency-dependent detector gain are presented.

## 6.1 Determination of modulation depth ( $a$ )

### 6.1.1 Model for laser-intensity spectra

The frequency modulation depth can be determined by simulating the intensity spectrum of a frequency- and intensity-modulated electric field and comparing that with measured intensity spectra [35, 40, 46]. The electric field and intensity spectrum of a frequency- and intensity-modulated laser beam can be modeled using Eqs. 9 through 12 [35].

$$E(t) = E_0(1 + M\cos(2\pi ft + \psi)) \times \exp(i2\pi c\nu_c t + i\beta\sin(2\pi ft)). \quad (9)$$

Here,  $E(t)$  is the time-varying electric field,  $E_0$  is the amplitude of the electric field without modulation,  $M$  is half of the DC-intensity-normalized intensity modulation amplitude (i.e.,  $M = i_0/2$ ),  $\nu_c$  [ $\text{cm}^{-1}$ ] is the carrier frequency of the laser light,  $f$  [Hz] is the modulation frequency,  $c$  [cm/s] is the speed of light,  $\psi$  is the phase shift between intensity- and frequency-modulation, and  $\beta$  is the ratio of modulation depth to modulation frequency (i.e.,  $\beta = a/f$  where  $a$  and  $f$  have units of Hz). This equation can be rewritten as an infinite series of exponential terms which describes the laser light as an electric field at the carrier frequency with a series of sidebands spaced by the modulation frequency. The frequency and magnitude of each electric field component are given by Eqs. 10 and 11, respectively.

$$\nu_k = \nu_c + kf/c \quad (10)$$

$$E_k = J_k(\beta) + \frac{M}{2i} e^{i\psi} J_{k-1}(\beta) - \frac{M}{2i} e^{-i\psi} J_{k+1}(\beta). \quad (11)$$

Here,  $k$  is an integer from  $-\infty$  to  $\infty$ ,  $\nu_k$  [ $\text{cm}^{-1}$ ] and  $E_k$  [a.u.] are the frequency and amplitude of the electric field,

respectively, at the  $k$ th harmonic of the modulation frequency, and  $J$  is the Bessel function of the first kind. In Eq. 11,  $f$  is divided by  $c$  such that all components have units of  $\text{cm}^{-1}$ . The intensity spectrum,  $I$ , is given by Eq. 12.

$$I = \sum_{k=-\infty}^{\infty} I_k = \sum_{k=-\infty}^{\infty} |E_k|^2. \quad (12)$$

### 6.1.2 Measurements of laser-intensity spectra

A scanning Fabry-Perot interferometer (FPI) with an FSR of 10 GHz and a spectral resolution of 67 MHz (Thorlabs SA210-12B) was used to measure intensity spectra of frequency- and intensity-modulated laser light. The interferometer operates by scanning the separation distance between two confocal spherical mirrors in order to selectively transmit a narrow band (set by FPI resolution) of optical frequencies. A photodetector is used to measure the intensity of each frequency [47]. Accurately modeling the measured intensity spectrum requires precise knowledge of the relative frequency axis of the data (obtained via calibration) and the instrument response function (IRF).

The relative frequency axis was determined as follows. Fixed-frequency laser light was directed into the FPI while it was scanned over its full FSR several times. In this case, one interference fringe (i.e., peak) appears each time the FPI has scanned 1 FSR (10 GHz here). A second-order polynomial was fit to each peak location (in time) in order to obtain a relative frequency axis.

Next, the FPI's IRF was determined experimentally by recording an intensity spectrum of fixed-frequency laser light (i.e., no modulation). The FPI's IRF is governed by the physical characteristics of the interferometer (e.g., resolution, finesse) and the coupling/alignment of the laser light into the cavity. As a result, the IRF was determined prior to each experiment that was conducted to characterize the frequency modulation amplitude in order to ensure that the IRF was accurate for each dataset.

The modulation depth of each TDL was determined by measuring the intensity spectrum of the frequency- and intensity-modulated laser light and least-squares fitting a simulated intensity spectrum to the measured spectrum. In the fitting routine, first an infinitely resolved intensity spectrum was calculated using Eqs. 11 and 12 (for example, see Fig. 5a) including a sufficient number of harmonics (i.e., values of  $k$ ) to span the measured spectrum. The infinitely resolved intensity spectrum was then convolved with the measured IRF and normalized by its peak value to produce the final intensity spectrum which was compared with the measured peak-intensity-normalized spectrum. The fitting routine employed the following free parameters:  $a$ ,  $\psi$ ,  $f$  (due to extreme sensitivity to this parameter), a constant intensity

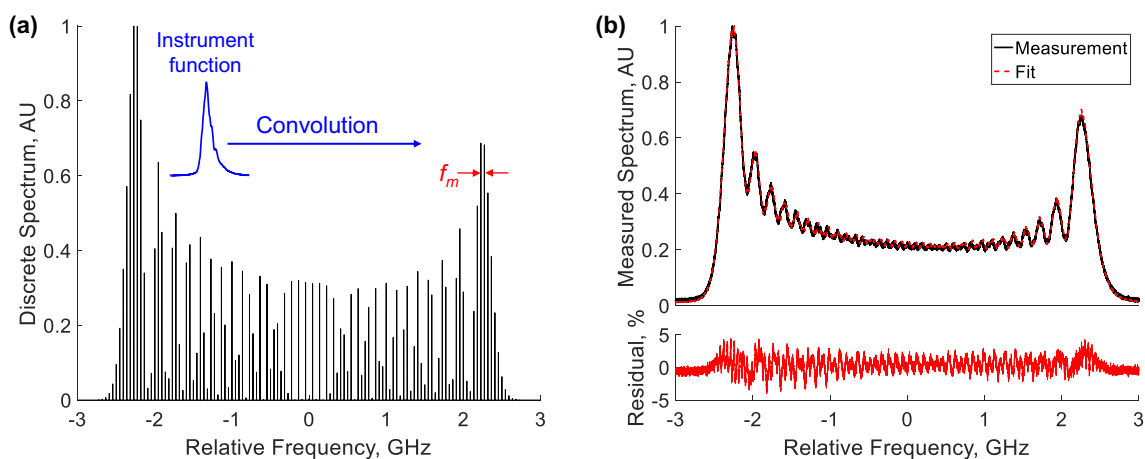


**Fig. 5** Simulation of discrete intensity spectrum and measured instrument function (a). Measured and best-fit intensity spectra corresponding to the TDL emitting near 1469 nm while being modulated with  $f$

$= 45.5$  MHz and  $a = 0.0795$   $\text{cm}^{-1}$  (b). The best-fit spectrum shown in (b) was obtained from the convolution of the discrete spectrum and measured instrument function shown in (a)

offset, and a constant relative frequency offset. Figure 5b shows an example of a measured and best-fit intensity spectrum corresponding to the TDL emitting near 1469 nm with  $f = 45.5$  MHz and  $a = 0.0795$   $\text{cm}^{-1}$ . The good agreement between the measured and simulated intensity spectra suggests that the model used to produce the best-fit spectrum is accurate and that the modulation depth obtained from the best-fit spectrum is accurate.

Of the parameters being varied in the fitting routine, the simulated spectrum and, therefore, quality of the fit is most sensitive to the modulation depth and modulation frequency. The overall width of a spectrum for a given modulation frequency is governed by the modulation depth and, therefore, a modulation depth that is accurate within 1% can be obtained even if each individual peak is not well resolved (i.e.,  $f$  is less than the FPI's resolution). Much smaller variations in modulation depth provide further tuning of the relative magnitude of each peak within a spectrum.

## 6.2 Determination of phase shift ( $\psi$ )

While Eqs. 9 and 11 are dependent on  $\psi$ , it was not possible to determine it with sufficient accuracy from the best-fit intensity spectra since they are relatively insensitive to  $\psi$ . To address this, measurements of the full scanned-WMS- $2f/1f$  spectrum for each transition were acquired in a heated static-gas cell using the same modulation parameters, but with a reduced scan rate (1 kHz) to minimize the influence of injection-current scanning on the laser's response to modulation. Simulated scanned-WMS- $2f/1f$  spectra were least-squares fit to the measured scanned-WMS- $2f/1f$  spectra following the general procedure given by Goldenstein et al. [22]; however,  $\psi$  was treated as an additional free parameter. The scanned-WMS- $2f/1f$

spectrum is significantly more sensitive to the phase shift than the laser's intensity spectrum (from FPI data). Ultimately, this enabled an accurate measurement of  $\psi$  to be obtained from the best-fit scanned-WMS- $2f/1f$  spectra. Figure 6 shows an example of measured and best-fit scanned-WMS- $2f/1f$  spectra that were used to determine  $\psi$  for the TDL emitting near 1392 nm with  $f=35$  MHz and  $a=0.107$   $\text{cm}^{-1}$ .

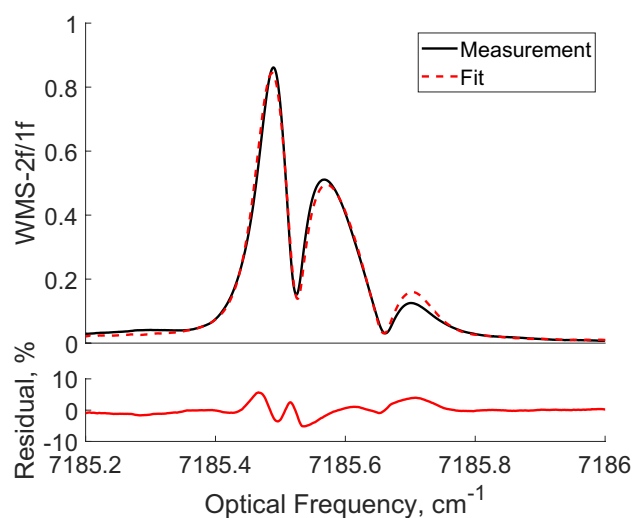


**Fig. 6** Example of measured and best-fit scanned-WMS- $2f/1f$  spectrum that was used to determine  $\psi$  for the TDL emitting near 1392 nm while modulated with  $f = 35$  MHz and  $a = 0.107$   $\text{cm}^{-1}$  and scanned at 1 kHz with a scan amplitude of  $0.512$   $\text{cm}^{-1}$ . For this measurement,  $L = 9.7$  cm,  $X_{\text{H}_2\text{O}} = 11.5\%$ , and  $T = 294$  K

### 6.3 Intensity tuning

While each laser's intensity response to the modulation waveform can often be characterized in the absence of the scan waveform [22], coupling between the scan and modulation waveforms can become non-negligible when the laser's current is scanned and modulated more aggressively (i.e., at larger frequencies and amplitudes). To account for this coupling, a time history of the intensity of the laser light was measured with a photodiode while the scan and modulation waveforms were simultaneously applied to the laser's injection current. During post-processing, the instantaneous value of  $i_0$  (i.e., the intensity modulation amplitude normalized by the local nominal intensity) for each modulation period was calculated to provide a measurement of the time-varying  $i_0$ . The value of  $i_0$  corresponding to the location of the transition linecenter within the wavelength scan was used in the WMS model to calculate WMS- $2f/1f$  signals at linecenter as a function of gas conditions. It is important to note that the value of  $i_0$  at linecenter differs between up-scans and down-scans due to the phase shift between intensity and wavelength scanning.

Accurately measuring  $i_0$  required precise alignment of the laser beam onto the center of the detector chip when modulating at the near-GHz frequencies used here. Misaligning the laser beam onto the edge of the detector chip caused  $i_0$  to decrease compared to the true value (obtained with the laser beam focused onto the center of the detector chip). This effect was never observed when using modulation frequencies on the order of 100s of kHz. Interestingly and fortunately, misalignment never impacted the magnitude of the WMS- $2f/1f$  signals. Regardless, error in the perceived  $i_0$  must be avoided since it would ultimately result in simulating WMS- $2f/1f$  signals (at a given thermodynamic condition) with a magnitude that is different than measured, thereby introducing systematic error into the measurement of gas conditions.

### 6.4 Detector frequency response

The detector's frequency response was measured to account for differences in the detector gain between the WMS- $1f$  and  $-2f$  signals. This is particularly important when the harmonics of the modulation frequency approach the detector bandwidth where pronounced variations in gain often exist. A frequency-swept waveform varying from 1 to 240 MHz was applied to a given laser's bias-T, and the laser's intensity time history was measured simultaneously on the 150 MHz bandwidth detector (Thorlabs PDA10CF) and on a second detector with a bandwidth from 1 MHz to 1 GHz (Menlo Systems FPD 310). The power spectrum of the 150 MHz detector (calculated from an FFT of the raw detector signal) was normalized by that of the 1 GHz detector to cancel out

the laser's frequency response and provide a measurement of the 150 MHz detector's frequency-dependent gain (see Fig. 7). This approach assumes that the 1 GHz detector has a frequency-independent gain at the frequencies of interest, and this assumption was found to be accurate based upon the scanned-WMS- $2f/1f$  measurements acquired at known gas conditions in the static-gas cell. The 150 MHz detector's response to each laser was characterized separately, and a small wavelength dependence was observed. For the laser emitting near 1392 nm (modulated at 35 MHz) and the laser emitting near 1469 nm (modulated at 45.5 MHz), the ratios of detector gain at the second and first harmonics (i.e.,  $G_{2f}/G_{1f}$ ) were 1.146 and 1.327, respectively.

## 7 Experimental results

### 7.1 Calculation of gas properties

The WMS- $1f$  and  $-2f$  signals were extracted from the raw detector signal during post-processing as described in [22]. Background subtraction was performed according to [21] to remove the signal components resulting from non-linear laser-intensity modulation and ambient absorption. The intensity time histories measured with the test gas and without the test gas (for the background measurement) were multiplied by reference cosine and sine waves at frequencies corresponding to each WMS harmonic and low-pass filtered to extract the  $X$ - and  $Y$ -components of each harmonic signal. Equation 13 was then used to calculate the background-subtracted WMS- $2f/1f$  signal.

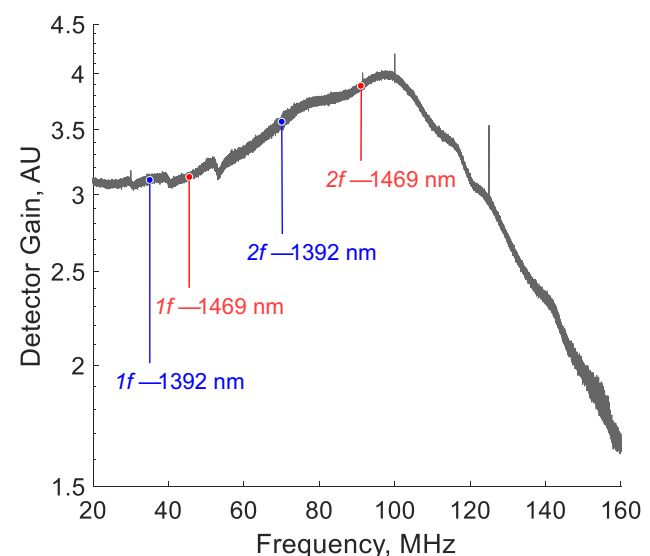


**Fig. 7** Measured relative detector gain of the Thorlabs PDA10CF detector near its 3 dB bandwidth (150 MHz)

$$\text{WMS-}2f/1f = \left[ \left[ \left( \frac{X_{2f}}{R_{1f}} \right)_{\text{raw}} - \left( \frac{X_{2f}}{R_{1f}} \right)_{\text{bg}} \right]^2 + \left[ \left( \frac{Y_{2f}}{R_{1f}} \right)_{\text{raw}} - \left( \frac{Y_{2f}}{R_{1f}} \right)_{\text{bg}} \right]^2 \right]^{1/2} \quad (13)$$

Here,  $R_{1f}$  is the root-sum-square of the X and Y components of the  $1f$  signal,  $X_{2f}$  and  $Y_{2f}$  are the X and Y components of the  $2f$  signal, and the subscripts *raw* and *bg* correspond to the data collected with and without the test gas, respectively. In addition, the measured WMS- $2f/1f$  signals were then divided by  $G_{2f}/G_{1f}$  to account for differences in the detector's frequency response between harmonics. Alternatively, this could be accounted for by multiplying the simulated WMS- $2f/1f$  signals by the measured  $G_{2f}/G_{1f}$ .

The path-integrated temperature of  $\text{H}_2\text{O}$  was determined by comparing the measured two-color ratio of scanned-WMS- $2f/1f$  signals (at the transition linecenters) to that predicted by the calibration-free WMS model [21] assuming a uniform line-of-sight with the known pressure and for an estimated bath gas composition (note: this two-color ratio is nearly independent of mole-fraction [21, 27]). As mentioned previously, the measured temperature is expected to agree within 1 to 4% of  $\bar{T}_{\text{H}_2\text{O}}$ . Once the temperature was determined at a given moment in time, the magnitude of the scanned-WMS- $2f/1f$  signal at the linecenter of the transition near  $7185.59 \text{ cm}^{-1}$  was used to determine the measured  $\text{H}_2\text{O}$  column density ( $N_{\text{H}_2\text{O}}$ ). This procedure was conducted iteratively (typically requiring 2 iterations) until the  $\text{H}_2\text{O}$  column density converged within 1% between iterations. It is important to note that the scanned-WMS- $2f/1f$  signals were simulated using the local value of  $i_0$  (obtained while the laser wavelength was scanned and modulated) at the transition linecenter. This enabled the use of the calibration-free WMS model developed by Rieker et al. [21] (which does not account for the influence of injection-current scanning on the laser parameters). In addition, the aforementioned calculations were performed separately for up-scan and down-scan signals due to their unique  $i_0$ .

## 7.2 Sensor validation

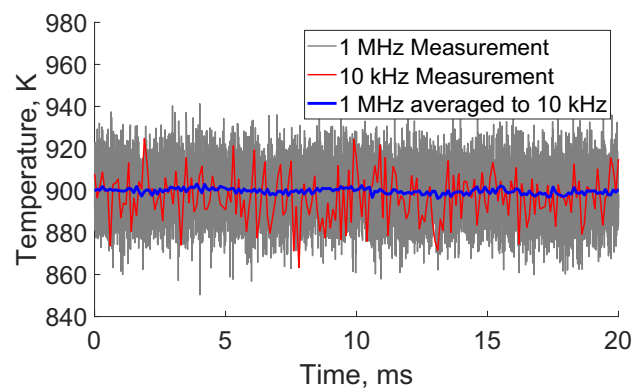
Measurements of temperature and  $\text{H}_2\text{O}$  concentration were acquired in a heated gas cell to validate the accuracy of the scanned-WMS- $2f/1f$  diagnostic employing near-GHz modulation frequencies and to compare its performance with that provided using more conventional modulation frequencies (i.e.,  $f < 1 \text{ MHz}$ ). Measurements were acquired in the static-gas cell described in [43] at 700–1200 K with  $\text{H}_2\text{O}$  concentrations ranging from 8 to 13% by mole at a pressure of 1 atm. WMS measurements were compared with the temperatures measured by type-K thermocouples and

the water concentration measured using scanned-DAS with the same lasers.

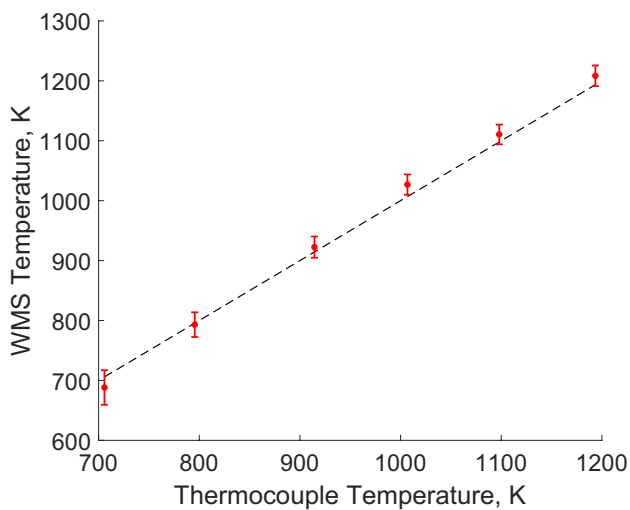
Figure 8 presents WMS measurements of gas temperature acquired in the static-gas cell while using different modulation frequencies. The measurements acquired at 1 MHz using modulation frequencies of 35 and 45.5 MHz exhibit a  $1-\sigma$  precision of 10.8 K, and the measurements acquired at 10 kHz using modulation frequencies of 35 and 45.5 kHz exhibit a slightly larger  $1-\sigma$  precision of 11.2 K. The results shown in Figure 8 also illustrate how time averaging the 1 MHz measurement down to 10 kHz improves the measurement precision to 1.7 K which is 6.5 $\times$  smaller than the 10 kHz measurement acquired using modulation frequencies of 35 and 45.5 kHz. This shows that, for a given final measurement rate, it is advantageous to use higher modulation and scan frequencies, likely because this can isolate signals from noise and enable additional time averaging.

Figure 9 presents a summary of the temperature measurements acquired using scanned-WMS- $2f/1f$  at 1 MHz in the gas cell at 700–1200 K. In all cases, the measured temperature is within 20 K of that measured by thermocouples. The error bars represent a  $2-\sigma$  precision in the measurement and demonstrate the sensor's high precision across a range of temperatures. For the data acquired at 900 K, the  $2-\sigma$  precision is 17.7 K and the absorbance was approximately 0.29 and 0.027 for the transitions near  $7185.59 \text{ cm}^{-1}$  and  $6806.03 \text{ cm}^{-1}$ , respectively. The measurement precision for this experiment is primarily limited by electronic noise from the detector and data acquisition system, a portion of which is passed by the large bandwidth lock-in filters.

In addition, across the range of conditions studied, the measured  $\text{H}_2\text{O}$  mole fraction agreed within 2–10% of the mole fraction measured with a 1 kHz scanned-DAS measurement. We suspect that baseline errors in the scanned-DAS



**Fig. 8** Comparison of scanned-WMS- $2f/1f$  measurements of gas temperature acquired at measurement rates of 1 MHz (with  $f=35$  or 45.5 MHz) and 10 kHz (with  $f=350$  or 455 kHz). The measurement acquired at 1 MHz and time averaged to 10 kHz exhibits 6.5 $\times$  smaller precision compared to the measurement acquired directly at 10 kHz



**Fig. 9** Scanned-WMS- $2f/1f$  measurements of gas temperature acquired in the static-gas cell at 1 atm and 700–1200 K. The results illustrate that the WMS measurements agree within 20 K of the known temperature (from thermocouples)

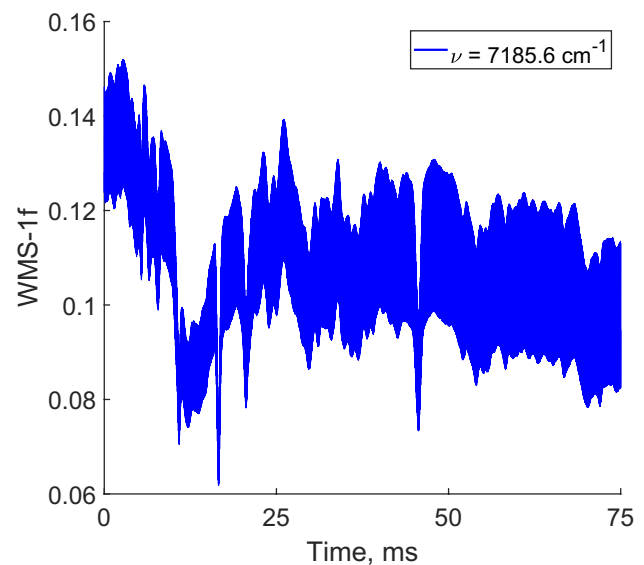
measurements are largely responsible for the differences in  $\text{H}_2\text{O}$  concentration measured by scanned-WMS- $2f/1f$  and scanned-DAS. In addition, time-varying adsorption of  $\text{H}_2\text{O}$  onto the walls of the inconel gas cell may also contribute to these differences since these measurements could not be conducted simultaneously.

### 7.3 HMX fireballs

Measurements of temperature and  $\text{H}_2\text{O}$  column density were acquired to characterize HMX fireballs with and without micro-aluminum ( $\mu\text{Al}$ ) particles and to demonstrate the sensor's ability to characterize dynamic, high-temperature combustion environments with large optical losses.

Figure 10 shows a time history of the WMS- $1f$  signal measured in a fireball of HMX and  $\mu\text{Al}$  using the TDL emitting near 1392 nm. The signal envelope results from the laser's intensity and, therefore  $i_0$ , varying sinusoidally at 500 kHz due to injection-current scanning. The magnitude of the  $1f$  signal is dominated by laser-intensity modulation when the absorbance is small ( $\alpha \ll 1$ ) as is the case here. As a result, variations in the  $1f$  signal occurring at  $f < 500$  kHz primarily result from optical losses due to beamsteering and particle scattering. Therefore, the  $1f$  signal can be used to estimate the optical density of the fireball along the line of sight. For the data shown, the minimum  $1f$  signal occurs at  $\approx 20$  ms and this corresponds to a maximum optical depth of 0.72 (calculated on a natural log basis).

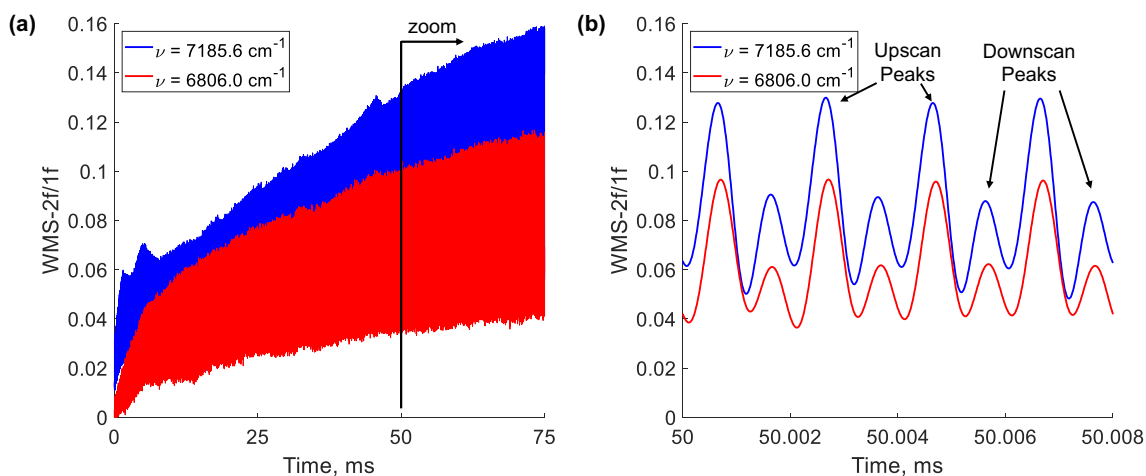
Figure 11a shows time histories of the WMS- $2f/1f$  signals measured in a fireball of HMX and  $\mu\text{Al}$ . In contrast to the WMS- $1f$  signal, the magnitude of the WMS- $2f/1f$  signals



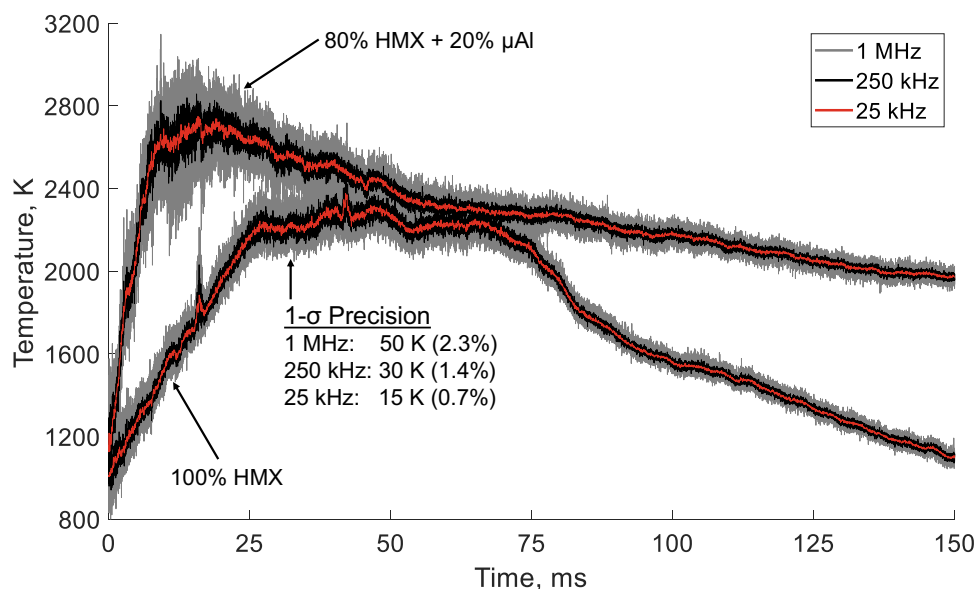
**Fig. 10** Time history of the WMS- $1f$  signal measured in a fireball of 80% HMX and 20%  $\mu\text{Al}$  by mass using the TDL emitting near 1392 nm. Variations in the WMS- $1f$  signal primarily result from non-absorbing transmission losses

exhibit a relatively smooth rise throughout the majority of the test time due to (1) fireball growth and some cooling which led to increased absorbance and (2) the use of  $1f$ -normalization to cancel out non-absorbing transmission losses. Figure 11b shows a zoom view of the WMS- $2f/1f$  signal time histories to demonstrate the signal structure and quality across several scans. The magnitude of the WMS- $2f/1f$  signal varies between up-scans and down-scans due to the phase lag between wavelength and intensity scanning and this is accounted for in the calibration-free WMS model that was used to determine gas properties as described in Sect. 6.3.

Figure 12 presents temperature time histories measured in fireballs of pure HMX and mixtures of 80% HMX and 20%  $\mu\text{Al}$  by mass. Due to varying ignition delay times between tests, time zero for each test was defined as the time where the WMS- $2f/1f$  signal for the laser emitting near 1469 nm was large enough to provide a reliable temperature measurement. The results are shown for a measurement rate of 1 MHz and with time averaging down to rates of 250 kHz and 25 kHz to improve measurement precision. The  $1-\sigma$  measurement precisions at the temperature plateau in the pure HMX fireball were 50 K, 30 K, and 15 K for measurement rates of 1 MHz, 250 kHz, and 25 kHz, respectively. These values of precision were achieved with an absorbance of 0.061 and 0.031 for the transitions near  $7185.6\text{ cm}^{-1}$  and  $6806.0\text{ cm}^{-1}$ , respectively. While there are additional sources of noise in fireball experiments (e.g., from beamsteering, particle scattering), the noise is applied to the raw intensity signal and is largely (but not completely) rejected by



**Fig. 11** Time histories of WMS-2f/1f signals that were measured in a fireball of 80% HMX and 20%  $\mu$ Al by mass (a). The zoom view shows the time-varying structure of the WMS-2f/1f signals and the peak values which are used for calculating gas properties (b)



**Fig. 12** Comparison of temperature time histories measured using scanned-WMS-2f/1f in a fireball of pure HMX and a fireball of 80% HMX and 20%  $\mu$ Al by mass. Both fireballs burned in an atmosphere of dry air. The aluminized fireball exhibits a larger peak temperature and sustains a temperature above 2000 K for much longer

utilizing  $1/f$  normalization. The larger measurement precision, compared to gas cell measurements, is primarily due to a reduction in absorbance (4.8 times smaller) for the transition near  $7185.6 \text{ cm}^{-1}$ . Based on the SNR of the WMS-2f/1f signal at the temperature plateau in the HMX fireball, the minimum detectable absorbance is  $6.3 \times 10^{-4}$  and  $6.2 \times 10^{-4}$  for the transitions near  $7185.6 \text{ cm}^{-1}$  and  $6806.0 \text{ cm}^{-1}$ , respectively, at a measurement rate of 1 MHz.

Immediately following ignition, the path-integrated temperature of  $\text{H}_2\text{O}$  increases at a rate of 60 K/ms in the pure HMX fireball and 260 K/ms for the HMX and  $\mu$ Al

fireball. This suggests that the aluminum leads to a more rapid and complete ignition event. In the pure HMX fireball, the temperature decreases below 2000 K at approximately 80 ms. In contrast, the temperature of the HMX and  $\mu$ Al fireball remains elevated above 2000 K for the duration of the test, thereby demonstrating an increase in burn duration as expected. In addition, the peak path-integrated temperature of  $\text{H}_2\text{O}$  was  $\approx 2700 \text{ K}$  for the HMX and  $\mu$ Al fireball, which is  $\approx 400 \text{ K}$  larger than the fireball of pure HMX. Collectively, these results support three key findings about the addition of 20 wt%  $\mu$ Al to HMX test

samples in the experimental apparatus studied here: this increased (1) the peak path-integrated temperature of  $\text{H}_2\text{O}$  in the fireball, (2) the energy release rate, and (3) the burn duration. It is important to note that these results may be specific to the experimental apparatus and procedure for initiating the fireballs. Most importantly, in our experience the geometry of the sample holder and the ignition voltage can influence how readily the sample ignites and, subsequently, the ensuing fireball expansion and mixing processes within the test chamber. That said, these variables were held constant in the tests discussed here.

Figure 13 compares time histories of  $\text{H}_2\text{O}$  column density scaled by temperature (i.e.,  $N_{\text{H}_2\text{O}} \times T$ ) which were measured in a fireball of pure HMX and a fireball of 80% HMX and 20%  $\mu\text{Al}$  by mass. The  $\text{H}_2\text{O}$  column density was scaled by temperature to remove the impact of temperature on number density and, therefore, highlight changes in  $N_{\text{H}_2\text{O}}$  due to production and transport of  $\text{H}_2\text{O}$ . The results are shown for a measurement rate of 1 MHz, along with time-averaging down to rates of 250 kHz and 25 kHz. The  $\text{H}_2\text{O}$  column density measured in the pure HMX fireball indicates that the fireball grows for the first 40 ms and that a quasi-steady ball of combustion gas exists in the line-of-sight from 40 to 70 ms. After which, cooler combustion products reach the line-of-sight as the gases cool and exhaust out of the combustion chamber.

In contrast, the  $\text{H}_2\text{O}$  column density measured in the fireball of HMX and  $\mu\text{Al}$  indicates that the fireball growth is more rapid and high-temperature combustion products are sustained in the measurement path for longer. These

results further support the conclusion that the addition of  $\mu\text{Al}$  increased the energy release rate during ignition and increased the burn duration of the fireball. In addition, the fact that the aluminized fireball exhibits larger column densities of  $\text{H}_2\text{O}$  and for a longer period of time suggests that the addition of aluminum improved the combustion efficiency of HMX particles. This could be explained by recognizing that burning aluminum particles can promote combustion due to their high flame temperatures ( $> 3000$  K) and by acting as local ignition sources for HMX particles.

## 8 Conclusions

The design of a two-color scanned-WMS- $2f/1f$  diagnostic and its application to characterizing the evolution of temperature and  $\text{H}_2\text{O}$  in HMX fireballs at rates up to 1 MHz were presented. Notably, this work demonstrates that the use of scanned-WMS- $2f/1f$  with near-GHz modulation frequencies provides two critical benefits for combustion applications: (1) the ability to measure gas temperature and species at higher rates (1 MHz here) and (2) improved measurement precision. In doing so, to the best of our knowledge, this work presented the first calibration-free WMS- $2f/1f$  measurements of gas properties acquired at rates greater than 100 kHz.

Achieving the aforementioned advancements required several technical challenges to be addressed. Most importantly, new methods for characterizing each TDL's

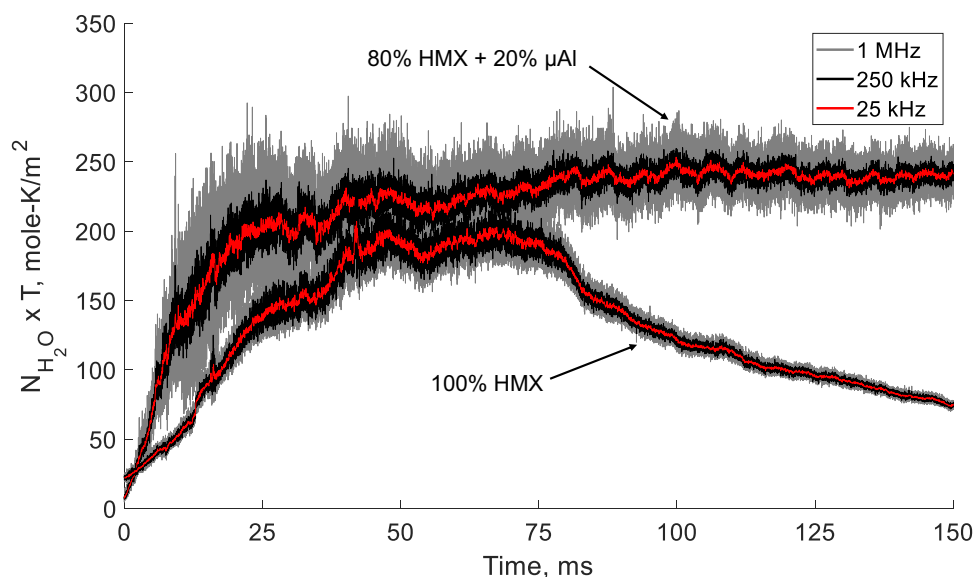


**Fig. 13** Comparison of  $\text{H}_2\text{O}$  column density time histories (scaled by temperature) measured using scanned-WMS- $2f/1f$  in a fireball of pure HMX and a fireball of 80% HMX and 20%  $\mu\text{Al}$  by mass. The results are scaled by temperature to normalize out variations in  $N_{\text{H}_2\text{O}}$  due to temperature and the results correspond to the temperature time histories shown in Fig. 12

wavelength and intensity response to near-GHz injection-current modulation were developed. The modulation depth of each laser was obtained from least-squares fitting simulated laser-intensity spectra to that measured using an FPI, and the phase shift between wavelength and intensity modulation was inferred from least-squares fitting simulated scanned-WMS- $2f/1f$  spectra to measured spectra. In addition, the frequency-dependent gain of the detector was characterized and accounted for to provide calibration-free WMS- $2f/1f$  measurements of gas properties using near-GHz modulation frequencies.

Measurements of temperature and H<sub>2</sub>O column density were acquired in fireballs of HMX (with and without aluminum) to demonstrate the sensor's ability to perform precise, high-bandwidth measurements in particle-laden combustion environments. In the fireball of pure HMX at  $\approx$  2300 K, 1- $\sigma$  precisions in temperature of 2.3%, 1.4%, and 0.7% were achieved at measurement rates of 1 MHz, 250 kHz, and 25 kHz, respectively. Similar results were obtained in the aluminized fireball. In addition, the results show that the addition of 20% (by mass) H-5 micro-aluminum led to (1) a more rapid ignition event, (2) a larger path-integrated fireball temperature (of H<sub>2</sub>O), and (3) combustion gas which sustained a high temperature (e.g., > 2000 K) for a longer duration. The measurements of H<sub>2</sub>O column density support these findings and, in addition, suggest that the addition of aluminum led to a greater combustion efficiency of HMX.

**Acknowledgements** This work was supported by a Defense Threat Reduction Agency (DTRA) Young Investigator Award (Grant: HDTRA1-17-1-0023) with Dr. Jeff Davis as program monitor. Garrett Mathews was supported by the National Science Foundation Graduate Research Fellowship Program (NSF GRFP, Grant: 1842166-DGE). The authors also thank Amanda Braun, Alex Brown, Mateo Gomez, Josh Ludwigsen, Prof. Steven Son, and Prof. Terrence Meyer at Purdue University for their assistance in preparing and handling test samples of HMX.

## References

- J.M. Peuker, P. Lynch, H. Krier, N. Glumac, Optical depth measurements of fireballs from aluminized high explosives. *Opt. Lasers Eng.* **47**(9), 1009–1015 (2009)
- R. Lodes, H. Krier, N. Glumac, Spectrally-and-temporally-resolved optical depth measurements in high explosive post-detonation fireballs. *Propellants Explos. Pyrotech.* **45**, 406–415 (2020)
- K.P. Brooks, M.W. Beckstead, Dynamics of aluminum combustion. *J. Propul. Power* **11**(4), 769–780 (1995)
- S. Goroshin, D.L. Frost, J. Levine, A. Yoshinaka, F. Zhang, Optical pyrometry of fireballs of metalized explosives. *Propellants Explos. Pyrotech.* **31**(3), 169–181 (2006)
- T. Bazyn, H. Krier, N. Glumac, Combustion of nanoaluminum at elevated pressure and temperature behind reflected shock waves. *Combust. Flame* **145**, 703–713 (2006)
- T. Bazyn, H. Krier, N. Glumac, Evidence for the transition from the diffusion-limit in aluminum particle combustion. *Proc. Combust. Inst.* **31**, 2021–2028 (2007)
- J.D. Koch, S. Piecuch, J.M. Lightstone, J.R. Carney, J. Hooper, Time-resolved measurements of near infrared emission spectra from explosions: Pure pentaerythritol tetranitrate and its mixtures containing silver and aluminum particles. *J. Appl. Phys.* **108**(3), 1–4 (2010)
- J.M. Peuker, P. Lynch, H. Krier, N. Glumac, On AIO emission spectroscopy as a diagnostic in energetic materials testing. *Propellants Explos. Pyrotech.* **38**(4), 577–585 (2013)
- N. Glumac, Absorption spectroscopy measurements in optically dense explosive fireballs using a modeless broadband dye laser. *Appl. Spectrosc.* **63**(9), 1075–1080 (2009)
- M. Soo, N. Glumac, Ultraviolet absorption spectroscopy in optically dense fireballs using broadband second-harmonic generation of a pulsed modeless dye laser. *Appl. Spectrosc.* **68**(5), 517–524 (2014)
- J.R. Carney, J.M. Lightstone, S. Piecuch, J.D. Koch, Water temperature and concentration measurements within the expanding blast wave of a high explosive. *Meas. Sci. Technol.* **22**, 045601 (2011)
- C. Murzyn, A. Sims, H. Krier, N. Glumac, High speed temperature, pressure, and water vapor concentration measurement in explosive fireballs using tunable diode laser absorption spectroscopy. *Opt. Lasers Eng.* **110**, 186–192 (2018)
- M.C. Phillips, B.E. Bernacki, S.S. Harilal, B.E. Brumfield, J.M. Schwallier, N.G. Glumac, Characterization of high-explosive detonations using broadband infrared external cavity quantum cascade laser absorption spectroscopy. *J. Appl. Phys.* **126**(9), 093102 (2019)
- C.S. Goldenstein, R.M. Spearrin, J.B. Jeffries, R.K. Hanson, Infrared laser-absorption sensing for combustion gases. *Prog. Energy Combust. Sci.* **60**, 132–176 (2017)
- K.D. Rein, S. Roy, S.T. Sanders, A.W. Caswell, F.R. Schauer, J.R. Gord, Measurements of gas temperatures at 100 kHz within the annulus of a rotating detonation engine. *Appl. Phys. B* **123**(3), 88 (2017)
- K.D. Rein, S. Roy, S.T. Sanders, A.W. Caswell, F.R. Schauer, J.R. Gord, Multispecies absorption spectroscopy of detonation events at 100 kHz using a fiber-coupled, time-division-multiplexed quantum-cascade-laser system. *Appl. Opt.* **55**(23), 6256–6262 (2016)
- E.F. Nasir, A. Farooq, Intra-pulse H<sub>2</sub>O absorption diagnostic for temperature sensing in a rapid compression machine. *Appl. Phys. B* **125**(11), 210 (2019)
- D.I. Pineda, F.A. Bendana, K.K. Schwarm, R.M. Spearrin, Multi-isotopologue laser absorption spectroscopy of carbon monoxide for high-temperature chemical kinetic studies of fuel mixtures. *Combust. Flame* **207**, 379–390 (2019)
- R.S. Chrystie, E.F. Nasir, A. Farooq, Towards simultaneous calibration-free and ultra-fast sensing of temperature and species in the intrapulse mode. *Proc. Combust. Inst.* **35**(3), 3757–3764 (2015)
- A.P. Nair, D.D. Lee, D.I. Pineda, J. Kriesel, W.A. Hargus, J.W. Bennowitz, S.A. Danczyk, R.M. Spearrin, Mhz laser absorption spectroscopy via diplexed rf modulation for pressure, temperature, and species in rotating detonation rocket flows. *Appl. Phys. B* **126**(8), 1–20 (2020)
- G.B. Rieker, J.B. Jeffries, R.K. Hanson, Calibration-free wavelength-modulation spectroscopy for measurements of gas temperature and concentration in harsh environments. *Appl. Opt.* **48**(29), 5546–5560 (2009)
- C.S. Goldenstein, C.L. Strand, I.A. Schultz, K. Sun, J.B. Jeffries, R.K. Hanson, Fitting of calibration-free scanned-wavelength-modulation spectroscopy spectra for determination of gas properties and absorption lineshapes. *Appl. Opt.* **53**(3), 356–367 (2014)



23. C.S. Goldenstein, R.M. Spearrin, I.A. Schultz, J.B. Jeffries, R.K. Hanson, Wavelength-modulation spectroscopy near 1.4  $\mu\text{m}$  for measurements of  $\text{H}_2\text{O}$  and temperature in high-pressure and-temperature gases. *Meas. Sci. Technol.* **25**(5), 055101 (2014)
24. R.M. Spearrin, C.S. Goldenstein, J.B. Jeffries, R.K. Hanson, Quantum cascade laser absorption sensor for carbon monoxide in high-pressure gases using wavelength modulation spectroscopy. *Appl. Opt.* **53**(9), 1938–1946 (2014)
25. C.S. Goldenstein, R.M. Spearrin, J.B. Jeffries, R.K. Hanson, Infra-red laser absorption sensors for multiple performance parameters in a detonation combustor. *Proc. Combust. Inst.* **35**(3), 3739–3747 (2015)
26. C.L. Strand, R.K. Hanson, Quantification of supersonic impulse flow conditions via high-bandwidth wavelength modulation absorption spectroscopy. *AIAA J.* **53**(10), 2978–2987 (2015)
27. C.S. Goldenstein, C.A. Almodóvar, J.B. Jeffries, R.K. Hanson, C.M. Brophy, High-bandwidth scanned-wavelength-modulation spectroscopy sensors for temperature and  $\text{H}_2\text{O}$  in a rotating detonation engine. *Meas. Sci. Technol.* **25**(10), 105104 (2014)
28. W.Y. Peng, S.J. Cassidy, C.L. Strand, C.S. Goldenstein, R.M. Spearrin, C.M. Brophy, J.B. Jeffries, R.K. Hanson, Single-ended mid-infrared laser-absorption sensor for time-resolved measurements of water concentration and temperature within the annulus of a rotating detonation engine. *Proc. Combust. Inst.* **37**(2), 1435–1443 (2019)
29. A. McLean, C. Mitchell, D. Swanston, Implementation of an efficient analytical approximation to the Voigt function for photoemission lineshape analysis. *J. Electron Spectrosc. Relat. Phenom.* **69**(2), 125–132 (1994)
30. C.S. Goldenstein, I.A. Schultz, J.B. Jeffries, R.K. Hanson, Two-color absorption spectroscopy strategy for measuring the column density and path average temperature of the absorbing species in nonuniform gases. *Appl. Opt.* **52**(33), 7950–7962 (2013)
31. J. Reid, J. Shewchun, B. Garside, E. Ballik, High sensitivity pollution detection employing tunable diode lasers. *Appl. Opt.* **17**(2), 300–307 (1978)
32. K. Sun, X. Chao, R. Sur, C.S. Goldenstein, J.B. Jeffries, R.K. Hanson, Analysis of calibration-free wavelength-scanned wavelength modulation spectroscopy for practical gas sensing using tunable diode lasers. *Meas. Sci. Technol.* **24**(12), 125203 (2013)
33. D.T. Cassidy, J. Reid, Atmospheric pressure monitoring of trace gases using tunable diode lasers. *Appl. Opt.* **21**(7), 1185–1190 (1982)
34. C.S. Goldenstein, I.A. Schultz, R.M. Spearrin, J.B. Jeffries, R.K. Hanson, Scanned-wavelength-modulation spectroscopy near 2.5  $\mu\text{m}$  for  $\text{H}_2\text{O}$  and temperature in a hydrocarbon-fueled scramjet combustor. *Appl. Phys. B* **116**, 717–727 (2014)
35. J.A. Silver, Frequency-modulation spectroscopy for trace species detection: theory and comparison among experimental methods. *Appl. Opt.* **31**(6), 707–717 (1992)
36. S. Kobayashi, Y. Yamamoto, M. Ito, T. Kimura, Direct frequency modulation in AlGaAs semiconductor lasers. *IEEE Trans. Microw. Theory Tech.* **30**(4), 428–441 (1982)
37. D. Welford, S. Alexander, Magnitude and phase characteristics of frequency modulation in directly modulated GaAlAs semiconductor diode lasers. *J. Lightwave Technol.* **3**(5), 1092–1099 (1985)
38. R.S. Tucker, High-speed modulation of semiconductor lasers. *IEEE Trans. Electron. Devices* **32**(12), 2572–2584 (1985)
39. R. Olshansky, P. Hill, V. Lanzisera, W. Powazinik, Frequency response of 1.3  $\mu\text{m}$  InGaAs high speed semiconductor lasers. *IEEE J. Quantum Electron.* **23**(9), 1410–1418 (1987)
40. C.S. Goldenstein, G.C. Mathews, Simulation technique enabling calibration-free frequency-modulation spectroscopy measurements of gas conditions and lineshapes with modulation frequencies spanning kHz to GHz. *Appl. Opt.* **59**(5), 1491–1500 (2020)
41. L.S. Rothman, I.E. Gordon, Y. Babikov, A. Barbe, D.C. Benner, P.F. Bernath, M. Birk, L. Bizzocchi, V. Boudon, L.R. Brown et al., The HITRAN2012 molecular spectroscopic database. *J. Quant. Spectrosc. Radiat. Transfer* **130**, 4–50 (2013)
42. C.S. Goldenstein, V.A. Miller, R.M. Spearrin, C.L. Strand, SpectraPlot.com: Integrated Spectroscopic Modeling of Atomic and Molecular Gases. *J. Quant. Spectrosc. Radiat. Transfer* **200**, 249–257 (2017)
43. K.K. Schwarm, H.Q. Dinh, C.S. Goldenstein, D.I. Pineda, R.M. Spearrin, High-pressure and high-temperature gas cell for absorption spectroscopy studies at wavelengths up to 8  $\mu\text{m}$ . *J. Quant. Spectrosc. Radiat. Transfer* **227**, 145–151 (2019)
44. R.J. Tancin, G.C. Mathews, C.S. Goldenstein, Design and application of a high-pressure combustion chamber for studying propellant flames with laser diagnostics. *Rev. Sci. Instrum.* **90**(4), 045111 (2019)
45. H. Li, G.B. Rieker, X. Liu, J.B. Jeffries, R.K. Hanson, Extension of wavelength-modulation spectroscopy to large modulation depth for diode laser absorption measurements in high-pressure gases. *Appl. Opt.* **45**(5), 1052–1061 (2006)
46. G.C. Bjorklund, Frequency-modulation spectroscopy: a new method for measuring weak absorptions and dispersions. *Opt. Lett.* **5**(1), 15–17 (1980)
47. M. Hercher, The spherical mirror Fabry-perot interferometer. *Appl. Opt.* **7**(5), 951–966 (1968)

**Publisher's Note** Springer Nature remains neutral with regard to jurisdictional claims in published maps and institutional affiliations.